Article

Nickel and Cobalt Ilmenites-Based Catalysts for Upgrading Pyrolytic Oil during Pyrolysis of Waste Tires

Daniela Correa-Muriel [1], Hoover Valencia-Sánchez [2], Héctor Cortes-Hernández [2], Daniela González-Vera [3], Javiera Herrera [3], Cristian H. Campos [3,*], Mónica L. Casella [1], Luis E. Arteaga-Perez [4] and Paula Osorio-Vargas [1,*]

[1] Centro de Investigación y Desarrollo en Ciencias Aplicadas "Dr. Jorge J. Ronco" (CINDECA), Departamento de Química, Facultad de Ciencias Exactas, UNLP-CCT La Plata, CICPBA, CONICET, 47 No. 257, La Plata 1900, Buenos Aires, Argentina
[2] Grupo de Investigación en Fotocatálisis y Estado Sólido, Escuela de Química, Universidad Tecnológica de Pereira, Pereira, Risaralda 660003, Colombia
[3] Departamento de Físico-Química, Facultad de Ciencias Químicas, Universidad de Concepción, Concepción 4030000, Chile
[4] Laboratory of Thermal and Catalytic Processes (LPTC), Wood Engineering Department, Faculty of Engineering, Universidad del Bio-Bio, Concepción 4030000, Chile
* Correspondence: ccampos@udec.cl (C.H.C.); paulaosorio@quimica.unlp.edu.ar (P.O.-V.)

Abstract: Pyrolysis as a waste treatment method has gained relevance because it can generate higher value-added products in addition to reducing the environment's secondary pollution. In this study, the catalytic pyrolysis of waste tires was evaluated using $NiTiO_3$ and $CoTiO_3$ ilmenites as catalysts and precursors of metal catalysts with the aim to produce an oil enriched in high-value hydrocarbons, such as benzene, toluene, a xylenes mixture, and products less-reported, such as *p*-cymene and *p*-cymenene. The experiments were performed in an analytical pyrolyzer coupled to GC/MS. The effect of the nature of the catalysts on the product distribution was compared with the uncatalyzed reaction. The main products of uncatalyzed pyrolysis were D, L-limonene (~60%), and isoprene (~25%) due to the depolymerization of natural rubber. Meanwhile, Ni-ilmenites-based catalysts favored the formation of target compounds to expense D, L-limonene. Moreover, the presence of metal in reduced-ilmenite sharply enhanced the selectivity by ~50% concerning oxidized ilmenite and above 80% compared to the uncatalyzed reaction for *p*-cymene and *p*-cymenene. By contrast, the Co-ilmenites-based catalysts showed a marginal effect on secondary reactions. Finally, the feasibility of forming the aromatic terpenes, *p*-cymene, and *p*-cymenene from limonene in the non-catalytic pyrolysis was evaluated.

Keywords: metal catalysts; ilmenites; waste tire pyrolysis; aromatics production

1. Introduction

Approximately one billion waste tires are generated annually worldwide [1]. The management, treatment, and disposal options for this type of residue include (i) material recovery as rubber, use of rubber particles in civil engineering applications, such as flooring in sports fields, and additive for asphalted routes, (ii) heat energy recovery via combustion, and, in some countries, (iii) disposal in landfills, converting them into disease vectors threatening human and ecosystems health [2]. In this sense, the pyrolysis of waste tires is a promising alternative for recycling, energy and fuel recovery, and even obtaining higher economic value products [3].

The polymeric fraction of the tire is constituted by a blend of two or three types of rubbers, namely natural rubber (NR), butadiene rubber (BR), and styrene–butadiene rubber (SBR). Three major product fractions are formed when this polymeric material is subjected to heat treatment at high temperatures (500–800 °C) in the absence of oxygen (pyrolysis).

A solid fraction (12–45%) conformed of recovered carbon black, which could be used as an adsorbent, catalyst, or substitute of carbon black; a gas fraction (10–35%) composed of C1–C4 hydrocarbons, CO, CO_2, and H_2, which is usually used as fuel in the same process (30–50 MJ m^{-3}); and a condensable fraction (35–65%).

The condensable fraction called tire pyrolytic oil (TPO) consists of a mixture of compounds such as D,L-limonene, isoprene, 4-vinylcyclohexene, benzene, toluene, mixed-xylene (BTXs), styrene, limonene isomer terpenes (γ- and α-terpinene and terpinolene), aromatic terpenes (*p*-cymene and *p*-cymenene) and some polycyclic aromatic hydrocarbons as naphthalene, among others. These compounds can be recovered and used as solvents, fuel additives, or intermediates in fine chemical synthesis. However, the viability of the process will depend on the economic value of the pyrolysis products. In this context, the development of catalytic pyrolysis was explored for TPO upgrading by increasing selectivity to high-value chemicals, such as BTXs [3–16], since the pioneering work developed by Williams et al. [17]. Zeolites have been the most-studied catalysts [5–9,17–19] for producing BTXs via pyrolysis. Their controllable properties, such as acidity (Si/Al ratio) and different pore channel structures and sizes, permit the design of the catalyst to produce these monoaromatic compounds selectively. Nevertheless, some reports have shown that their high density and strength of acid sites could favor the formation of PAHs, and coke deposition, leading to rapid catalyst deactivation.

Another high-value chemical compound that has also gained attention for being produced from waste tire pyrolysis is the *p*-cymene. This compound is used as a solvent and intermediate in fine chemical synthesis to produce fragrances, flavorings, and *p*-cresol. In addition, it could become a replacement for *p*-xylene in the preparation of terephthalic acid [20,21]. Some interesting results have been published recently about the formation of *p*-cymene during pyrolysis. Recently, Tavera-Ruiz et al. [22] and Osorio-Vargas et al. [13] showed high selectivity of this aromatic terpene using catalysts based on heteropolyacids supported on different oxides carriers. Both works attributed the catalytic activity to a greater Lewis/Bronsted acidity ratio.

All these targeted compounds arise from secondary reactions occurring during the pyrolysis, such as isomerization, dehydrogenation, aromatization, C-C bond breaking, and dealkylation. These reactions can be promoted by either acid sites, metal sites, or bifunctional catalysts, as we have shown in previous work [13–16]. Nevertheless, despite significant findings, further efforts are required to increase selectivity toward these products by using more selective catalysts and understanding their role in the reaction pathways.

Therefore, this study evaluates the use of Ni and Co ilmenites-binary oxides ($NiTiO_3$ and $CoTiO_3$) as catalysts [23,24] and precursors of supported metal catalysts to upgrade TPO. Using crystalline structures as catalyst precursors has become an effective method of obtaining catalysts with well-distributed and sintering-resistant metallic particles [25,26]. Accordingly, catalytic pyrolysis reactions were carried out in an analytical pyrolyzer, sought to promote secondary reactions leading to the formation of BTXs, *p*-cymene, and *p*-cymenene (benzene, 1-methyl-4-1-methylethenyl or dimethylstyrene). This latter compound is a valuable co-monomer for polystyrene production and related polymers, making its recovery from waste products attractive [27,28]. To the best of our knowledge, very few reports in the literature mention *p*-cymenene as a product of waste tire pyrolysis. In addition to evaluating the effect of catalysts on the formation of these compounds, an attempt was made to understand the reaction pathways that favor their formation.

2. Results and Discussion

2.1. Characterization of Feedstock and Catalysts

The elemental and proximate analysis of waste tires is presented in Table 1. Elements such as nitrogen, sulfur, and zinc, which are used during tire fabrication, were detected in the sample. The carbon content was around 79%, of which the organic carbon susceptible to decomposition corresponded to 58.8%. The evaluation of this volatile matter's different stages of decomposition was carried out by thermogravimetric analysis (TGA)

measurements, as seen in Figure S1. Five events were clearly detected by derivative thermogravimetry peaks. The first peak, around 230 °C, was attributed to the decomposition of the most volatile matter, such as plasticizers and additives. Afterward, the greatest mass loss was observed at approximately 400 °C, followed by a slight shoulder centered at 450 °C, assigned to the decomposition of natural rubber (NR) and styrene–butadiene rubber (SBR), respectively. Between 500 and 600 °C, the last two observed events are associated with the thermal degradation of more stable polymeric structures deriving from polybutadiene rubber (BR) and SBR. These observations agree with other reported work [29,30]. The mass loss between 200 °C and 600 °C was around 59.4%, which is consistent with the volatile matter determined by proximate analysis.

Table 1. Characterization of waste tire samples by proximate and elemental analysis.

Proximate Analysis (wt%)		Elemental Analysis			
		(wt%)		(mg kg^{-1})	
Moisture content	1.2	C	79.54	Al	955
Volatile matter	58.8	H	7.33	Ca	2687
Fixed carbon	30.2	N	0.47	Fe	4164
Ash	9.89	S	1.48	K	706
		O [1]	2.77	Zn	1121
		Si	883	Na	396

[1] Oxygen is calculated by the difference between C, H, N, S, and ash.

2.2. Catalyst Characterization

The formation of Ni and Co-ilmenites and the reduction effect on the structure were evaluated by X-ray diffraction (XRD) (Figure 1). In the oxidized Ni catalyst (Figure 1a), ilmenite structure was confirmed since the signals coincidence with the diffraction pattern of $NiTiO_3$ (JCPDS 33-0960), whose peaks were found at 2θ = 24.2°, 33.2°, 35.7°, 40.9°, 49.5°, 54.11°, 57.5°, 62.55°, and 64.17°, which can be assigned to the (012), (104), (110), (113), (024), (118), (211), (214), and (300) planes, respectively. In contrast, the reduced catalyst did not present the ilmenite phase. In this case, the diffraction pattern showed peaks of metallic Ni at 2θ: 44.09°, 51.70°, and 76.09° attributable to the (111), (200), and (220) lattice planes (JCPDS 04-0850). Regarding the oxidized Co catalyst (Figure 1c), this exhibited the ilmenite structure corresponding to $CoTiO_3$ (JCPDS 77-1373)) with peaks at 2θ: 23.74°, 32.60°, 35.19°, 40.32°, 48.83°, 53.28°, 56.60°, 61.72°, 63.35°, 70.46°, 74.72°, associated to crystal planes (012), (104), (110), (113), (024), (116), (122), (214), (300), (101), and, (220), respectively. Furthermore, the reduced Co catalyst displayed peaks corresponding to metallic Co at 2θ: 44.19°, 51.48°, and 75.82° related to (111), (200), and (220) planes, respectively (JCPDS 15-0806), without the presence of the ilmenite phase.

Both reduced catalysts exhibited a rutile-TiO_2 phase (JCPDS 75-1753) due to the total evolution of the ilmenite-type phases to the rutile phase of titanium dioxide with the Ni and Co metal fully reduced. The final composition of reduced materials was determined by the Rietveld method using Fullprof. Upon refinement, the existence of unreduced ilmenite was discarded. Figure 1b shows the refinement graph for the reduced $NiTiO_3$. Two phases were confirmed, a rutile type phase corresponding to 60.51% in the tetragonal crystalline system with space group $P4_2/mnm$ No. 136, and with the following lattice parameters, a = 4.59229 Å and c = 2.95874 Å. A metallic nickel phase equivalent to 39.49%, with a cubic crystalline system, space group Fm-3m No. 225, and lattice parameter a, equal to 3.52605 Å. The refinement plot for the reduced $CoTiO_3$ (Figure 1d) also demonstrated the presence of the phases due to rutile and metallic cobalt. The content of metallic cobalt was 45.79% and exhibited a cubic crystalline system, space group Fm-3m No. 225, and a lattice parameter, a = 3.54699 Å. The difference in some diffractions for the observed and calculated patterns confirms the surface presence of metal supported in the rutile phase for both materials.
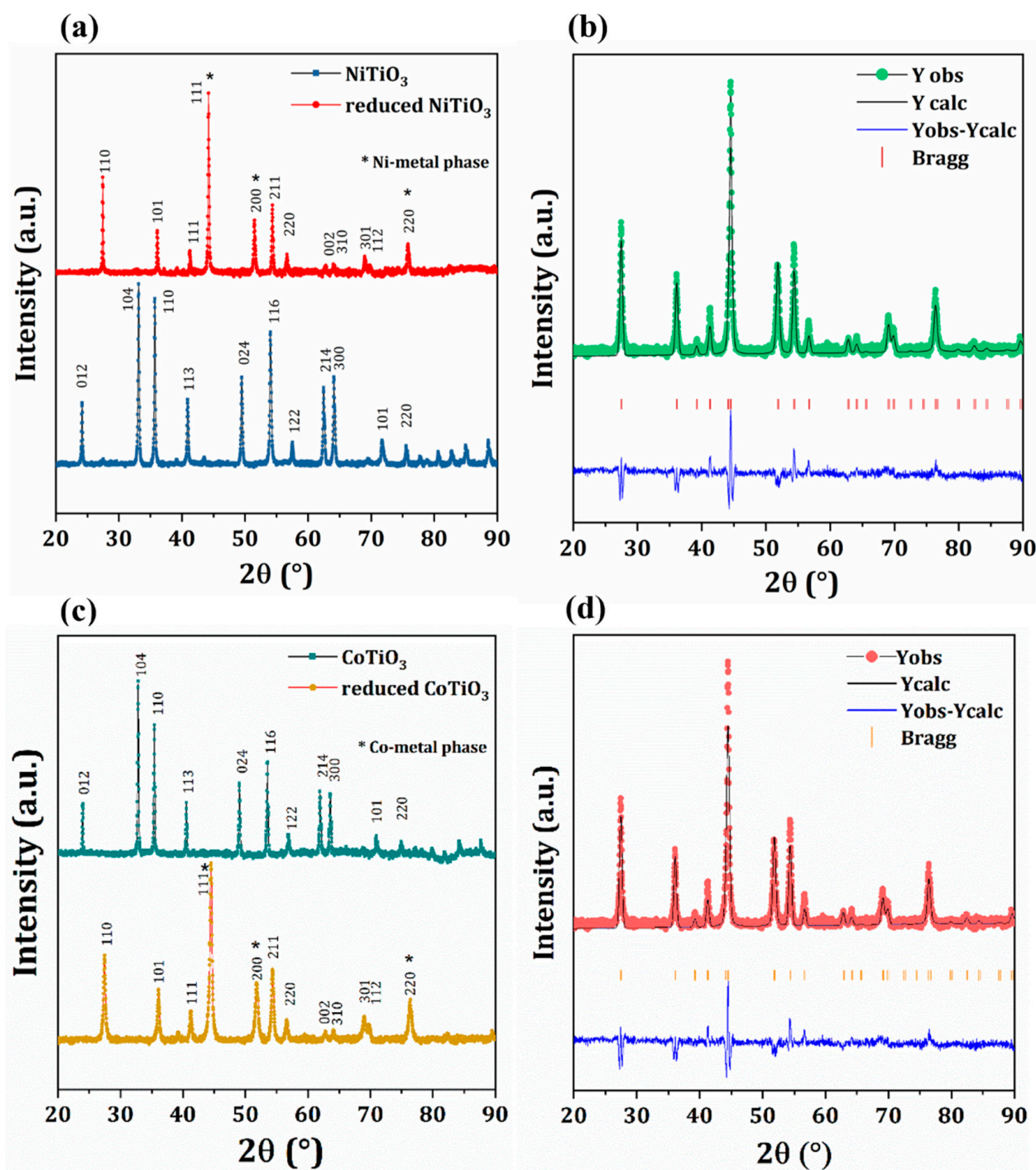
Figure 1. X-ray diffraction patterns for ilmenites-based catalysts of (**a**) Ni and (**c**) Co and refinement plots for (**b**) reduced $NiTiO_3$ and (**d**) reduced $CoTiO_3$.

The N_2 adsorption–desorption isotherms are shown in Figure S2. According to IUPAC classifications [31], the adsorption isotherms for all samples resemble a Type V isotherm with an H3-type hysteresis. This hysteresis type that was observed in the higher pressure range is indicative of non-rigid aggregates of plate-like particles or pore networks consisting of macropores [31]. The specific surface areas determined by the Brunauer–Emmett–Teller (BET) method for $NiTiO_3$, reduced $NiTiO_3$, $CoTiO_3$, and reduced $CoTiO_3$ were 12.4 m^2 g^{-1}, 13.3 m^2 g^{-1}, 12.2 m^2 g^{-1}, and 14.7 m^2 g^{-1}, respectively. The reduction treatment did not significantly affect the areas of the catalysts. The observed features were consistent with the morphologies determined by transmission electron microscopy (TEM) micrographs.

Figure 2a–d show that ilmenite-based catalysts (oxidized and reduced) exhibit a micro-rods structure consisting of agglomerates of micro- and nanoparticles with an average size between 800 and 1800 nm in length and 170 and 600 nm in width.
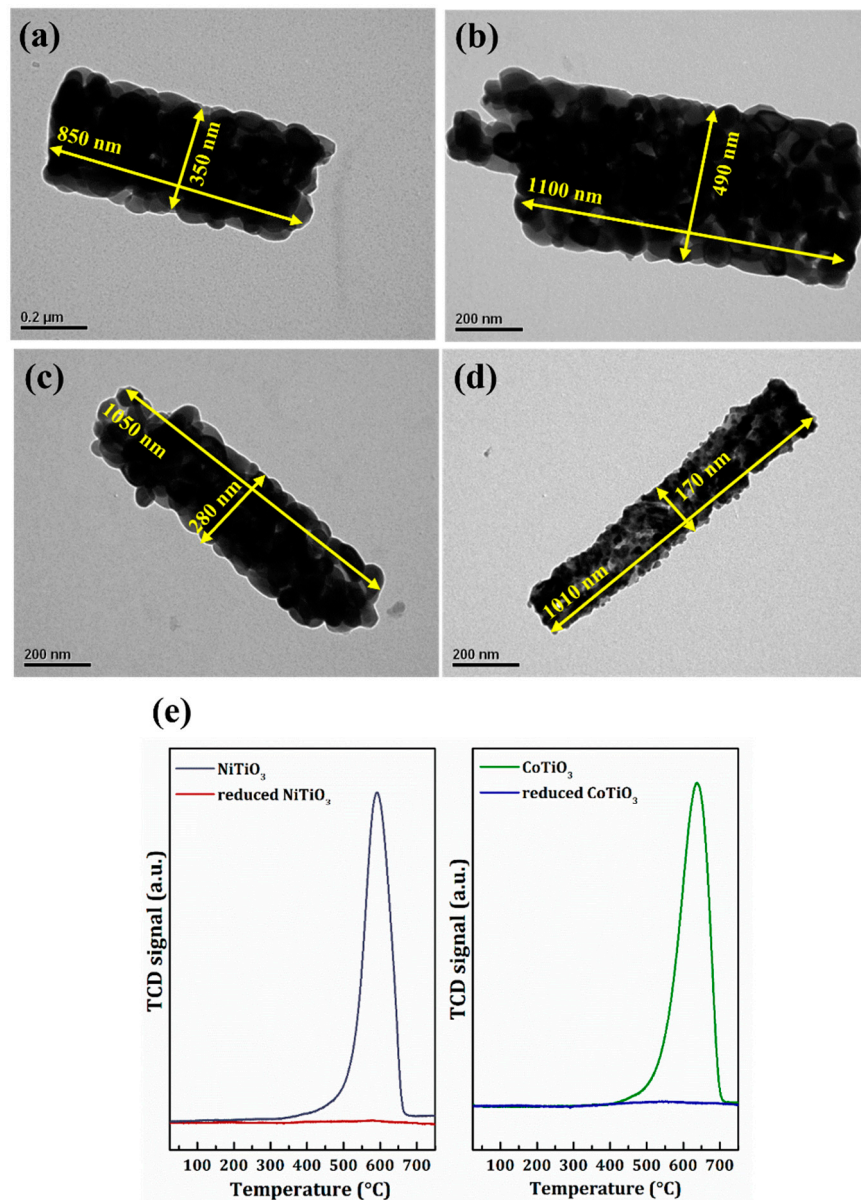

Figure 2. TEM micrographs of (**a**) $NiTiO_3$, (**b**) reduced $NiTiO_3$, (**c**) $CoTiO_3$, (**d**) reduced $CoTiO_3$ and (**e**) H_2-TPR profiles of the synthesized materials.

Moreover, the reductive treatment did not modify the micro-rod shape and dimensions. On the other hand, in H_2-TPR profiles (Figure 2e) for Ni and Co-ilmenites, a single peak of reduction was detected, which was assigned to the reduction of the corresponding cation (Ni and Co) embedded in the ilmenite crystal lattice. The second H_2-TPR realized for in situ reduced fresh ilmenites (Co and Ni) displayed no new signals in both cases, confirming a complete reduction in these cations after reductive treatment at 500 °C.

The chemical states of Ni and Co metals after reducing treatments were studied with X-ray photoelectron spectroscopy (XPS). The Co 2p spectrum of reduced $CoTiO_3$ is shown in Figure 3a. The deconvolution indicates that six peaks form the spectrum. Peaks at 778.9 and 793.8 eV for Co $2p_{3/2}$ and Co $2p_{1/2}$ correspond to metallic Co. Meanwhile, those peaks centered at 782.2 eV (Co $2p_{3/2}$) and 796.4 eV (Co $2p_{1/2}$) could be assigned to Co^{2+}. The

other two peaks belong to shake-up satellite peaks. The presence of the oxidized species can be due to the oxidation of the sample surface [2].
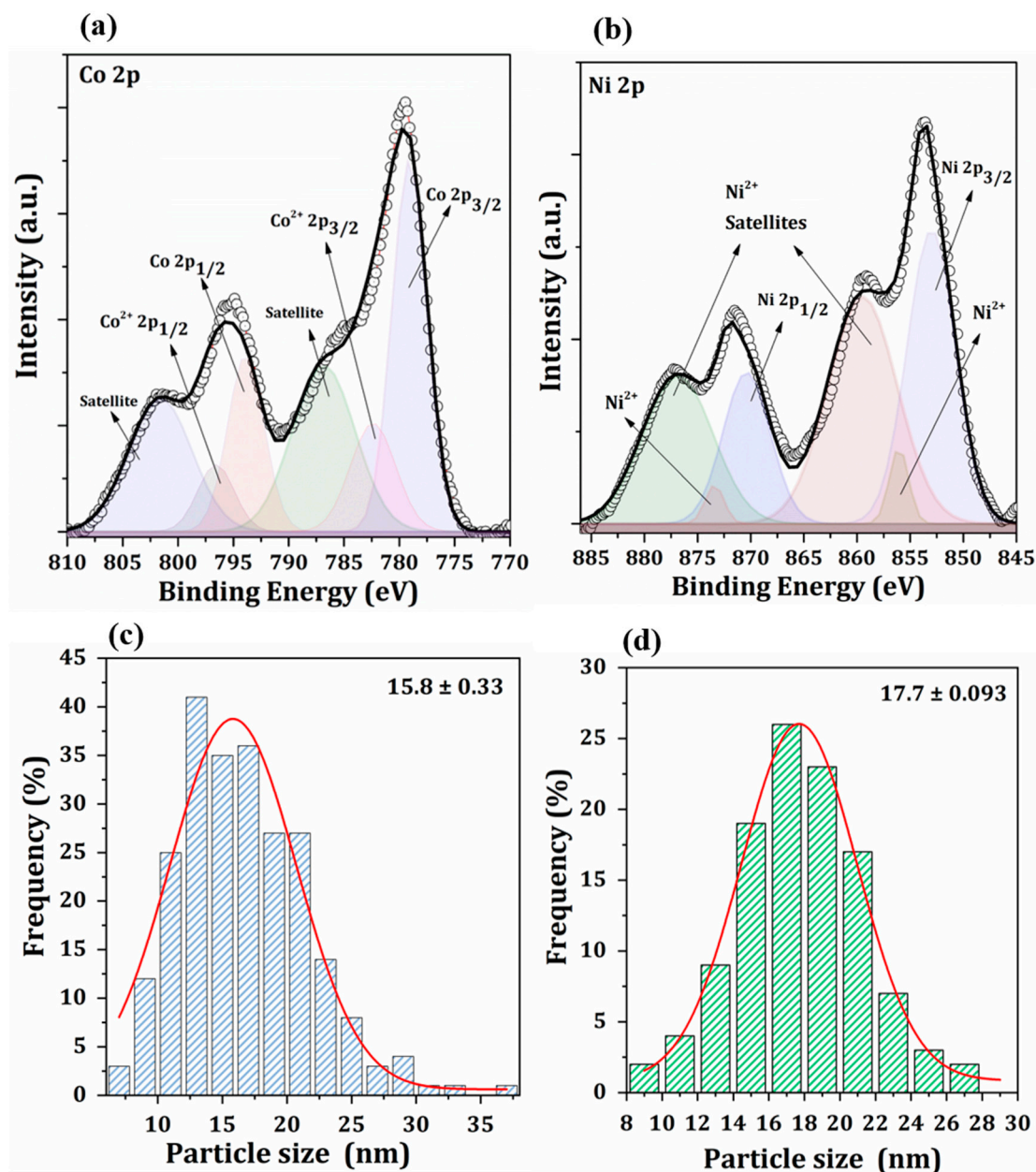
Figure 3. X-ray photoelectron spectra (XPS) for (**a**) Co 2p, (**b**) Ni 2p and particle size distribution for (**c**) Co metal, (**d**) Ni metal in reduced ilmenites.

The binding energies (BE) of the Ni 2p in reduced $NiTiO_3$ catalyst were located at 853 and 870.3 eV for 2p3/2 and 2p1/2 states, respectively (Figure 3b), which agree with the value reported in the literature for metallic Ni [32,33]. The fitting peaks at 855.9 eV and 873.3 eV correspond to Ni^{2+}, while the two broad peaks at 859.6 and 877 eV were assigned as divalent nickel (Ni^{2+}) satellites [32,33]. These oxidized species appear mainly due to the air oxidation of subsurface Ni atoms during the analysis. The XRD and XPS analysis demonstrated the existence of metallic Ni and Co in the catalysts subjected to the reduction treatment. Finally, TEM microscopy and Scherrer equation permitted the determination of the metal particle size. Figure 3c,d show the distribution of particle sizes for Ni and Co in reduced ilmenites as determined by TEM (Figure S3). The distribution was similar for both materials, with an average size of 15.8 and 17.7 nm for Co and Ni, respectively. The particle

size evaluated by XRD showed a similar trend, with slightly larger sizes, 18 nm for Co and 25 nm for Ni. The differences may be due to the broadening of the XRD peak cannot be attributed purely to the size of the crystal [34].

2.3. Pyrolysis Reaction of Waste Tires Carried out in a Py-GC/MS System

2.3.1. Main Products and Reaction Pathways during Uncatalyzed Pyrolysis Reaction of Waste Tires and Their Components (NR, BR, SBR)

The product distribution obtained from waste tire pyrolysis (Figure 4) was measured at 400 °C, according to the TGA results. The main reaction products under noncatalytic conditions were D,L-limonene (~60%), and isoprene (~ 25%) (Figure 4a). These products are mainly obtained from cracking reactions on natural rubber's C-C bonds (377.4 kJ mol^{-1}) [35], as the results in Figure 4d suggest.
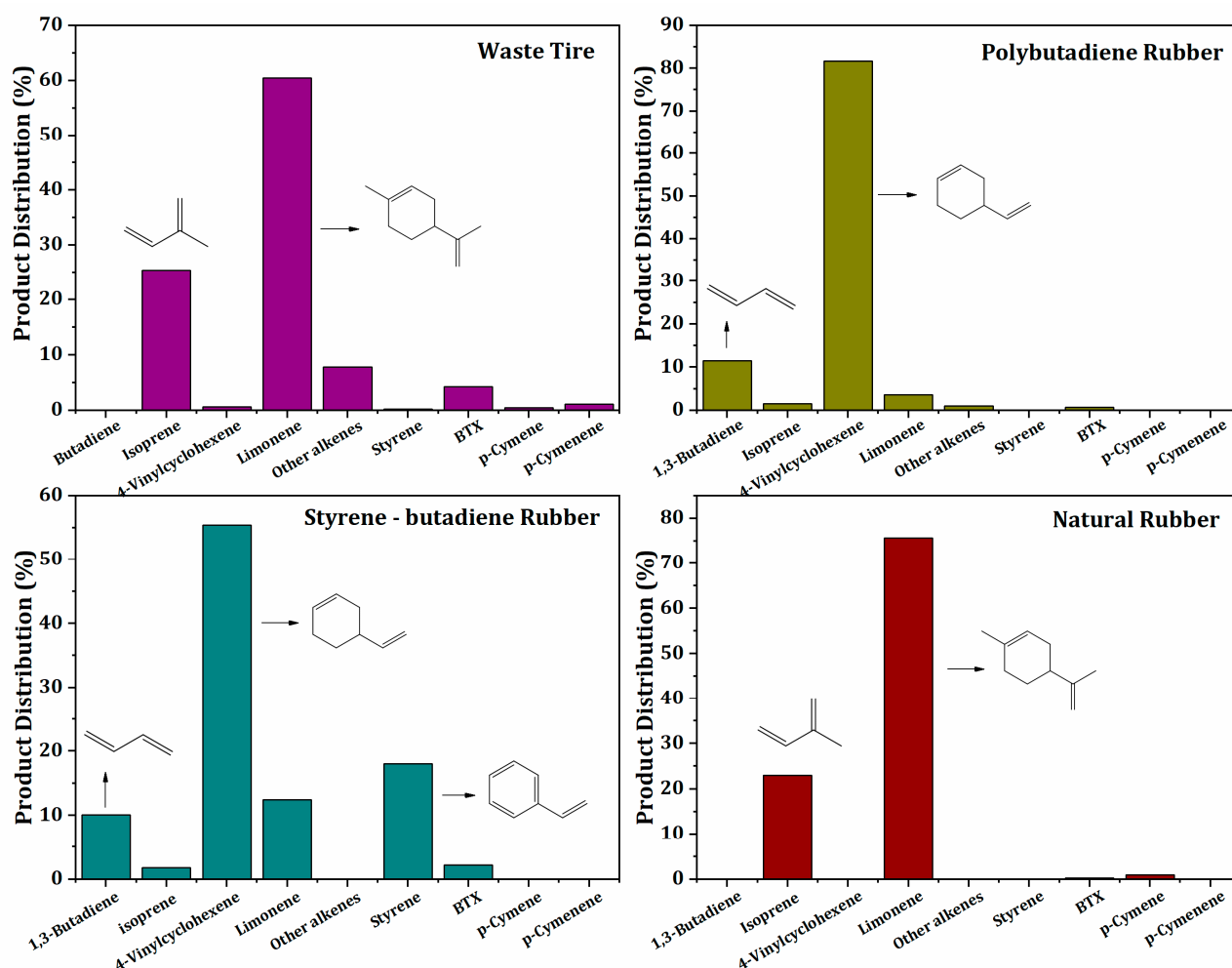
Figure 4. Pyrolysis of waste tires and their components carried out at 400 °C. Main reaction products.

Limonene is generated through a radical reaction initiated by homolytic breaking the β bond with respect to the double bonds of the main polymer chain. This rupture involves the formation of two radical chains (Scheme 1), which undergoes an intramolecular cyclization yielding D,L-limonene, and 1,5-dimethyl-5-ethenyl-cyclohexene [15,36]. The highest amount of D,L-limonene obtained is attributed to the methyl group's steric hindrance and higher radical stability by hyper-conjugation [37]. In addition, both radicals can unzip toward the monomer isoprene. *p*-Cymene and *p*-cymenene (Figure 4a) were produced by secondary reactions involving D,L-limonene as was demonstrated in previous studies [16]. This latter may undergo isomerization reactions, giving rise to the formation of terpinolene and α and γ-terpinene, which were detected in the pyrolysis products (classified as other

alkenes). Subsequently, these terpenes can undergo dehydrogenation reactions to produce the corresponding *p*-cymene and/or *p*-cymenene products (Scheme 1).

(a)

(b)
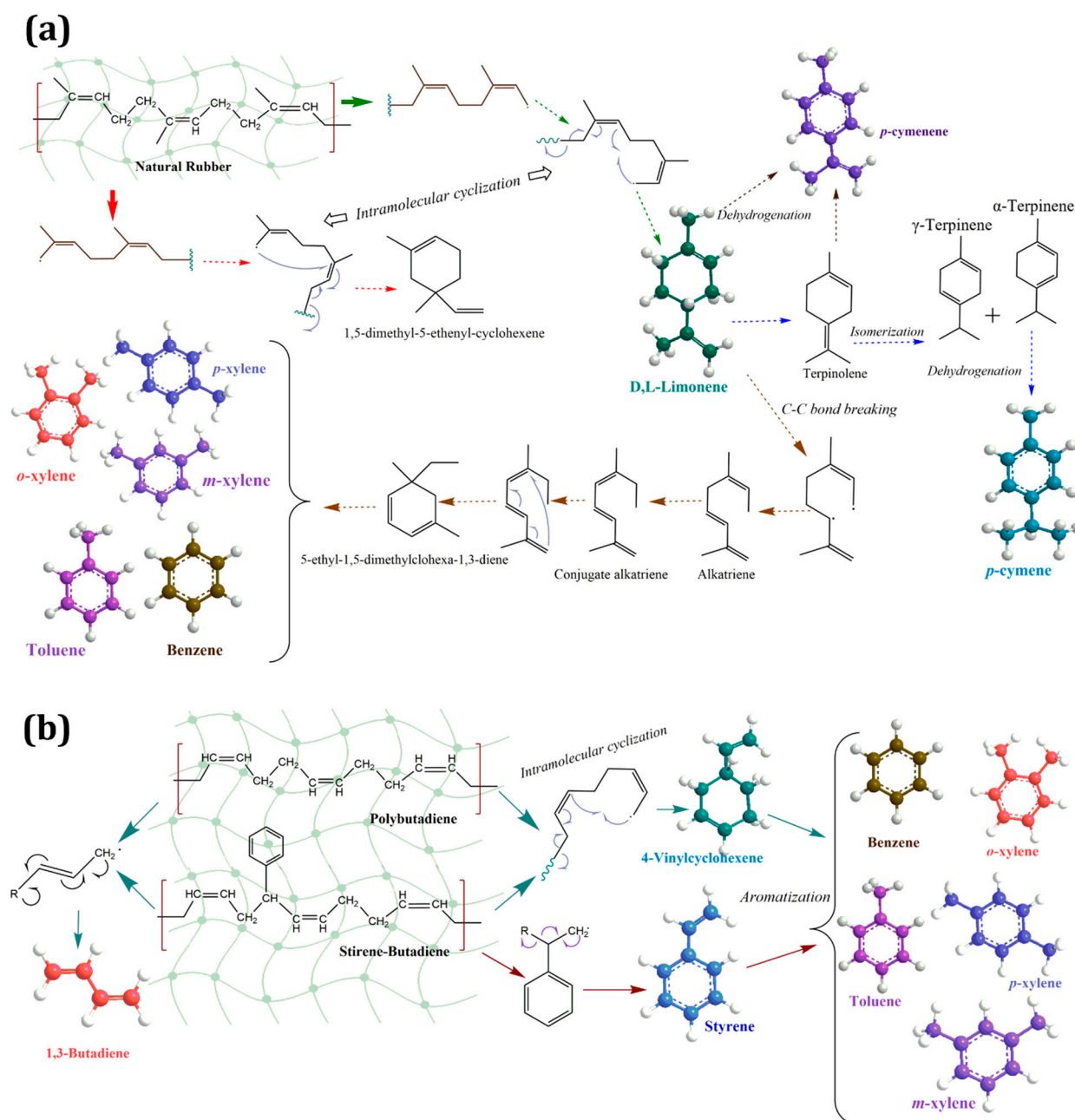
Scheme 1. Reaction pathways during pyrolysis reaction of tire components (**a**) natural rubber, (**b**) polybutadiene rubber, and styrene–butadiene rubber.

In addition, under reaction conditions, the D,L-limonene may undergo scission of the C-C bond in the β position of the limonene ring, giving rise to a diradical diene (Scheme 1). This radical is transformed into an alkatriene by intramolecular hydrogen transfer, whose isomerization to its conjugate form and succeeding cyclization resulted in some cylcloalkenes identified in the reaction products as 5-ethyl-1,5-dimethylclohexa-1,3-diene and 1,5,5,6-tetramethyl 1,3-cyclohexadiene (classified as other alkenes). Then, aromatization reactions lead to the mentioned aromatic compounds. Therefore, the aromatic compounds such as BTXs, *p*-cymene, and *p*-cymenene, detected mainly in tires, are formed

from secondary reactions of isomerization, dehydrogenation, and C-C bond scission that occur on the identified cycloalkenes in the reaction products (Scheme 1).

When the pyrolysis reaction was conducted on BR and SBR, common products such as 1,3-butadiene and 4-vinylcyclohexene were obtained (Figure 4b,c), which come from polymer chain cleavage and posterior intramolecular cyclizations, as shown in Scheme 1b. Styrene was found mainly as a product of styrene–butadiene rubber depolymerization, while 1,3-butadiene derives from the depolymerization of both elastomers. The BTXs detected in the reaction products (Figure 4b,c) come from secondary reactions affecting 4-vinylcyclohexene, as another primary product from pyrolysis (Scheme 1b). This compound undergoes reactions of isomerization and dehydrogenation, forming ethylbenzene, as was demonstrated in [13]. Meanwhile, subsequent dealkylation reactions occurring on this latter can lead to BTXs (Scheme 1b).

2.3.2. Computational Study of Secondary Reactions Occurring on D,L-Limonene for the Formation of Aromatic Terpenes (*p*-Cymene and *p*-Cymenene)

Very few studies have focused on forming *p*-cymene and *p*-cymenene from the pyrolysis of waste tires. Usually, most of them are related to the production of BTXs. We recently presented interesting results on the selective formation of *p*-cymene from waste tires using TPA catalysts supported on TiO$_2$ [4]; however, we did not explore the formation of *p*-cymenene. Considering the importance of both terpenes and the intermediary character of the *p*-cymenene, we theoretically evaluated the feasibility of forming the aromatic terpenes, *p*-cymene, and *p*-cymenene, from limonene using density functional theory (DFT) calculations.

The possible mechanism is presented in Figure S4, without considering a catalyst or thermal effects. This was evaluated by the natural bond orbital (NBO), which was used to calculate the electron density distribution in atoms associated with bonds. NBO shows the electron population change as the molecule's chemical environment changes (Figure 5).
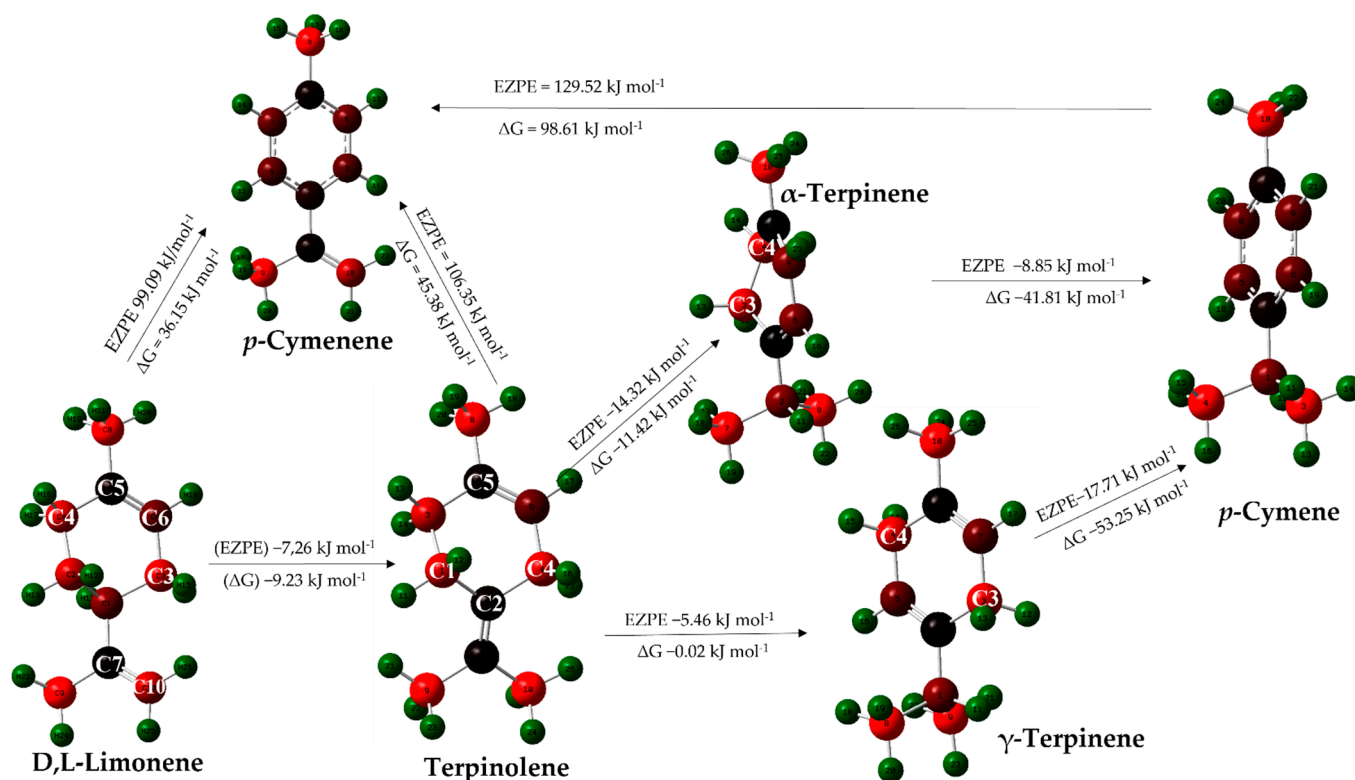
Figure 5. Distribution of NBO populations and energy differences of the molecules in the reaction mechanism. For NBO populations, the color variation (light red to light green) indicates a maximum negative charge of −0.65e for light red and a maximum positive charge of 0.65e for green.

The results showed that the D,L-limonene-to-terpinolene step is favored by 1,3-sigmatropic hydrogen shift, owing to that, charge distribution in the C10 atom (Figure 5) is larger than for the double ring bond located between C5 and C6. Furthermore, the theoretical energy differences validated the feasibility of this isomerization, which, for zero-point corrections, were EZPE = -7.26 kJ mol^{-1} and Gibbs free energy (ΔG) = -9.23 kJ mol^{-1}. The subsequent reaction stage from terpinolene to α-terpinene or γ-terpinene was also energetically favorable, with EZPE = -14.32 kJ mol^{-1} and -5.46 kJ mol^{-1}, ΔG = -11.42 kJ mol^{-1} and -0.02 kJ mol^{-1}, respectively.

However, it is observed that due to the charge transfer phenomena by conjugating the double bonds in the ring, the α-terpinene allows a higher stabilization in the 1,3-sigmatropic arrangement. This result would indicate that it is possible to expect a major amount of this isomer among the products. Moreover, in the natural bond orbital (NBO) population analysis for terpinolene, it was observed that C1 (migration position for the γ-isomer) and C4 (migration position for the α-isomer) exhibited similar values. However, C4 had a slightly higher population than C1 (Figure 5), favoring the arrangement toward the α-isomer. According to the mechanism proposed (Figure S4), *p*-cymene can be obtained from α-terpinene or γ-terpinene. Nevertheless, the dehydrogenation of γ-terpinene is more energetically favorable than α-terpinene, EZPE = -17.71 kJ mol^{-1} and -8.85 kJ mol^{-1}, ΔG = -53.25 kJ mol^{-1} and -41.81 kJ mol^{-1}, respectively. In the α-isomer, it is observed (Figure 5) that the carbon atoms C3 and C4 are charge-deficient, which would promote hydrogen loss by dehydrogenation; however, the NBO charge values on these atoms are lower due to the charge-transfer phenomena by conjugated double bonds compared to γ-terpinene. In this isomer, the C3 and C4 increase the charge deficiency 3-fold, making them slightly more favorable for dehydrogenation.

Concerning *p*-cymenene, three possible steps were postulated for its formation (Figure S4) from D,L-limonene (EZPE = 99.09 kJ/mol, ΔG = 36.15 kJ mol^{-1}), terpinolene (EZPE = 106.35 kJ mol^{-1}, ΔG = 45.38 kJ mol^{-1}), and p-cimene (EZPE = 129.52 kJ mol^{-1}, ΔG = 98.61 kJ mol^{-1}). In all cases, the energy values were unfavorable, which indicates that for their formation, it is required to carry out the reaction at a certain temperature or under the presence of a catalyst or to increase the retention time, letting secondary reactions take place (e.g., slow pyrolysis). However, the values obtained here show that D,L-limonene could be more easily dehydrogenated than terpinolene and *p*-cymene. In the population analysis, limonene does not require an isomerization step by a 1–3 sigmatropic arrangement as was proposed for terpinolene or carbons with similar charge density (C3 and C4, Figure 5) for dehydrogenation. In fact, in the limonene ring, charge-deficient carbons near carbons with higher electron density could facilitate this reaction step toward the direct formation of *p*-cymenene. The formation of *p*-cymenene was proposed to take place from *p*-cymene catalytic dehydrogenation [38]. Nevertheless, Horrillo-Martinez et al. [27] and Sanchez-Vazquez et al. [28] demonstrated that the aromatization of limonene could occur, retaining the exocyclic double bond giving rise to *p*-cymenene by using Pd(OTFA)$_2$ or Pd(OAc)$_2$ as catalysts. The direct dehydrogenation of D,L-limonene to *p*-cymenene would avoid the intermediate *p*-cymene and its subsequent high-temperature dehydrogenation to *p*-cymenene. Our results would point to this direct reaction being the most likely, which could be promoted by a temperature increase or a catalyzed reaction. Nonetheless, the increase in temperature did not significantly promote the compound's production, as seen in Figure S5.

Additionally, the reaction routes leading to *p*-cymene were confirmed as described in Scheme 1a. Since both compounds *p*-cymene and *p*-cymenene are used as intermediates in fine chemical synthesis, it would be interesting to produce them from the waste tire pyrolysis by favoring a selective transformation of limonene into these products during the pyrolysis reaction.

2.3.3. Effect of the Oxidized and Reduced Ilmenites on Secondary Reactions during Pyrolysis of Waste Tires

The effect of using ilmenites-based catalysts of $NiTiO_3$ and $CoTiO_3$ (oxidized and reduced) on secondary reactions during waste tire pyrolysis was studied at 400 °C and a feedstock/catalyst ratio of 1:2 (Figure 6). This temperature was selected because, under uncatalyzed pyrolysis, the D,L-limonene was more abundant (Figure S5). Therefore, as D,L-limonene is considered the main precursor of the expected high-value compounds (*p*-cymene, *p*-cymenene, and BTXs), this is the most feasible condition for inspecting the target secondary reactions.
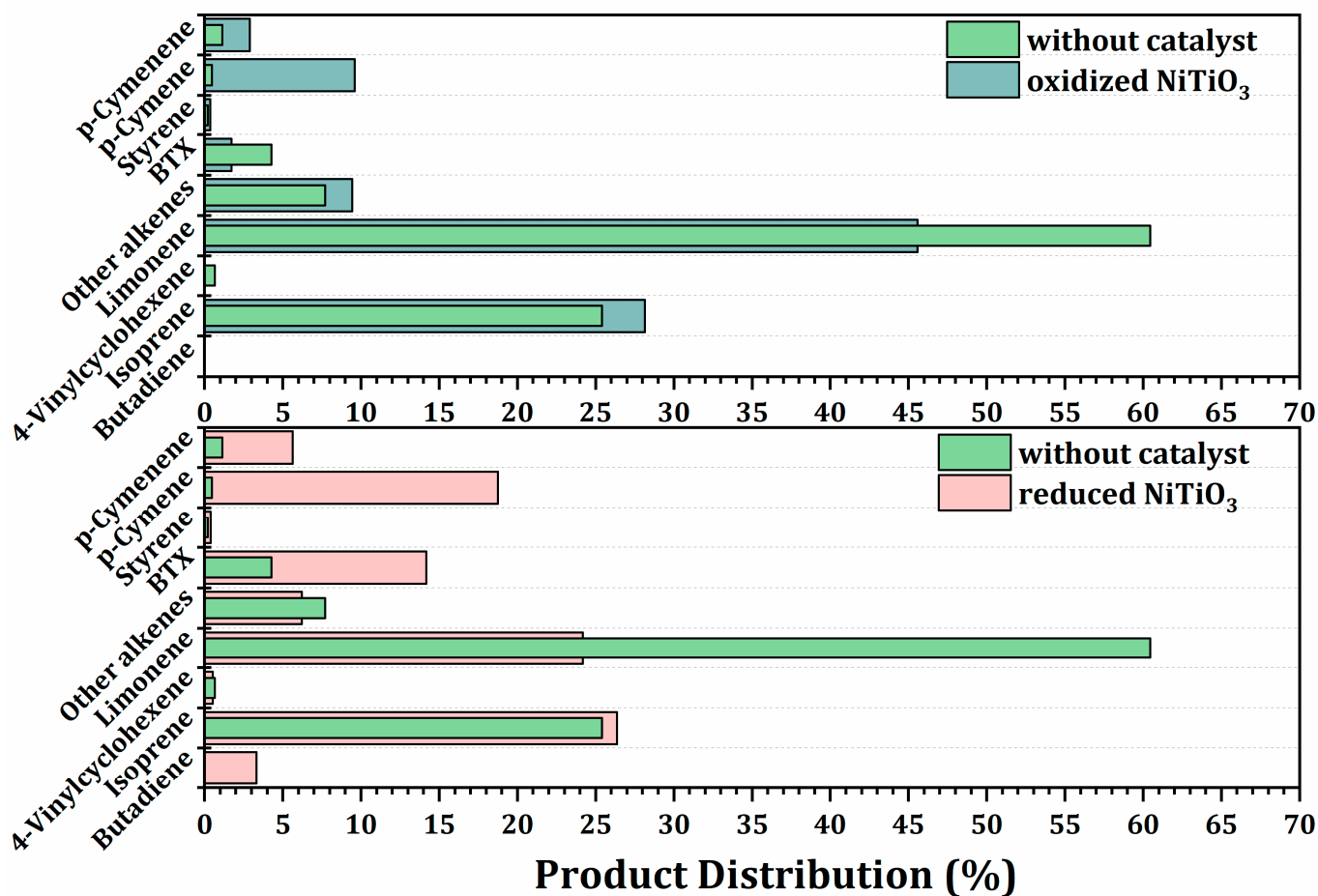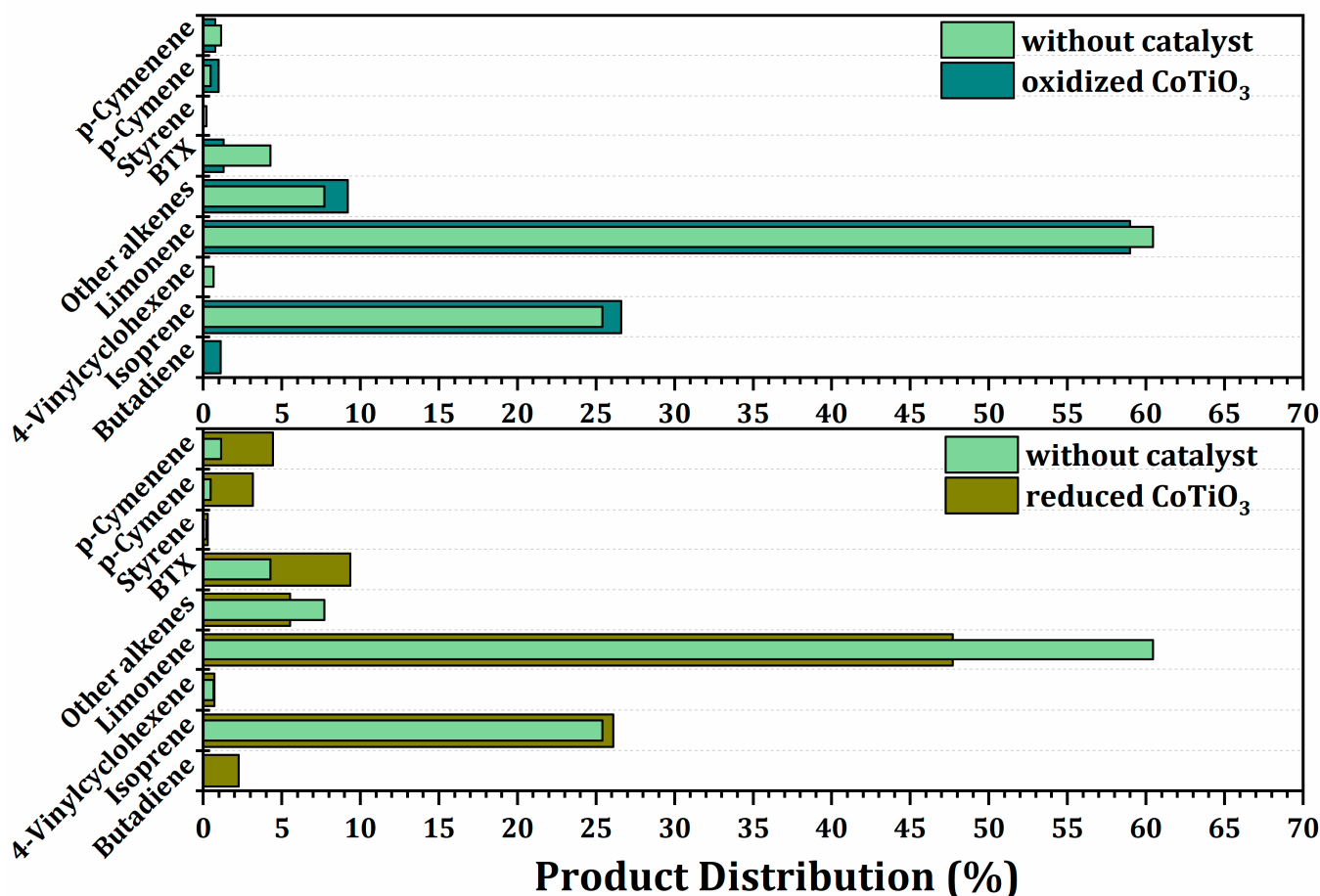

Figure 6. Effect of using oxidized and reduced $NiTiO_3$ on product distribution during WTP carried out a 400 °C. Feedstock/Catalyst ratio: 1:2.

It was observed that the product distribution from catalytic pyrolysis was different as compared to the uncatalyzed reaction. The oxidized $NiTiO_3$ ilmenite promoted the formation of *p*-cymene and *p*-cymenene (Figure 6), probably at the expense of limonene, since a decrease in its selectivity was observed. In contrast, no effect on BTXs formation was detected. Moreover, using reduced $NiTiO_3$ sharply enhanced the formation of aromatic terpenes. The reduced ilmenite increased *p*-cymene selectivity by 50% concerning oxidized ilmenite and by 97% compared to the uncatalyzed reaction.

Meanwhile, *p*-cymenene's rise was 48% and 80% concerning oxidized ilmenite and without catalyst, respectively. In addition, the reduced $NiTiO_3$ also favored the formation of BTXs (incremented by 70% as compared to the uncatalyzed reaction). On the contrary, when the oxidized $CoTiO_3$ was used, there was no significant difference with respect to the reaction without a catalyst, suggesting that this catalyst has a marginal effect on secondary reactions (Figure 7). Nevertheless, the $CoTiO_3$ reduction improved its catalytic activity

without being better than the NiTiO$_3$-reduced catalyst. On this catalyst, the presence of metal after reduction also favored the formation of *p*-cymene, *p*-cymenene, and BTXs.

Figure 7. Effect of using oxidized and reduced CoTiO$_3$ on product distribution during WTP carried out a 400 °C. Feedstock/catalyst ratio: 1:2.

The main secondary reactions occurring during uncatalyzed pyrolysis are isomerization and dehydrogenation (Scheme 1 and Section 2.2). Both groups of reactions can be promoted by the presence of acid and metallic sites or bifunctional acid/metal catalysts [39]. On acid sites (primarily Lewis's acid sites), two possible pathways for isomerization reactions can occur, one involving the formation of carbonium ions, and the other corresponds to the allyl route involving carbanions. A primary carbonium ion is formed through the adsorption of the extracyclic double-bond of D,L-limonene on acid sites, followed by a proton shift leading to a tertiary carbonium ion from which terpinolene could be generated. In turn, this compound can also be adsorbed in the same way, forming secondary and tertiary carbonium ions that lead to α and γ-terpinene

At the same time, olefins can be adsorbed on metal sites by electron donation from their π-orbitals to d-type orbitals of metal centers and simultaneous electro back-donation from full d-type orbitals of metal to empty π*-antibonding orbitals [40]. The terpene, thus adsorbed, can undergo isomerization reactions, leading to aliphatic terpenes. Finally, dehydrogenation reactions are favored on metallic sites. Therefore, the bifunctional character of reduced catalysts studied here could favor these secondary reactions and promote the formation of high-value hydrocarbons, such as BTXs, *p*-cymene, and *p*-cymenene compared with mixed oxide (oxidized ilmenite). Indeed, in previous work using Ni and Co catalysts supported over SiO$_2$ [15], the selectivity to *p*-cymene was much lower than that found here. These results demonstrated that using more acidic supports, such as TiO$_2$, increased almost by 90% the formation of this aromatic terpene by reduced NiTiO$_3$ and CoTiO$_3$ catalysts

compared to Ni/SiO$_2$ and Co/SiO$_2$, respectively, being in all cases higher for Ni catalysts. The differences in the catalytic activity between Co and Ni are related to the metal's nature since, as shown in the characterization, there were no significant differences in the physicochemical characteristics between both reduced catalysts. Therefore, the observed differences can be ascribed to the higher dehydrogenation capacity of Ni, as has been reported before [40].

It is noteworthy to mention that the presence of acid sites and bifunctional catalysts favor isomerization reactions, leading to the formation of limonene isomers (terpinolene and α- and γ-terpinene), which by dehydrogenation lead to the formation of *p*-cymene (Section 2.2), as we observe here and in our previous work [13–16,41]. Furthermore, according to the results obtained in Section 2.2, to promote the formation of *p*-cymenene, it is required to favor dehydrogenation rather than isomerization.

3. Materials and Methods

3.1. Materials and Chemical Reagents

The granules of waste tires were provided by a local company, and they were crushed and sieved into particle sizes between 180 and 300 μm before use. Tetrabutyl titanate (Ti(CH$_3$(CH$_2$)$_3$O)$_4$), nickel(II) acetate (Ni(CH$_3$COO)$_2$), cobalt(II) acetate (Co(CH$_3$CO$_2$)), pure elastomers (cis-1,4-polyisoprene, cis-polybutadiene and styrene-butadiene), D,L-Limonene (≥95%), benzene (≥99.9%), *o*-xylene (≥99.0%), *m*-xylene (≥99.5%), *p*-xylene (≥99.5%), toluene (≥99.9%) and *p*-cymene (≥99.5%) were supplied by Sigma Aldrich. Isopropanol, absolute ethanol, and ethylene glycol were provided by Merck. The reagents were used for synthesis without further purification. Gases used in reduction and reaction were supplied by Linde Chile, H$_2$ (99.99%), He (99.99%), N$_2$, and synthetic air.

3.2. Characterization of Waste Tires

All samples were subjected to proximate analysis for volatile matter, moisture content, ash content, and fixed carbon in a muffle furnace (Thermo Scientific F6020C, Boston, MA, USA) using the ASTM D3172 standard method. Elemental analysis of raw material was carried out in a Leco CHNS 628 elemental analyzer following the ASTM D5291 Standard method. Afterward, the composition of inorganic elements was measured in an inductively coupled plasma–optical emission spectrometry (ICP-OES) (PerkinElmer (Cambridge, MA, USA) Optima 7000 DV ICP-OES series instrument following the UNE En 15290 and 15297 method. Thermogravimetric analyses of material decomposition were measured in a Shimadzu TGA 50 Thermobalance.

3.3. Catalyst Synthesis and Characterization

3.3.1. Preparation of the Catalysts

CoTiO$_3$ and NiTiO$_3$ solids were synthesized using a modified protocol reported in [42]. A stoichiometric amount of Ni(CH$_3$COO)$_2$, Co(CH$_3$COO)$_2$, and Ti(CH$_3$(CH$_2$)$_3$O)$_4$ with the cationic ratio (Co, Ni)/Ti = 1 was dissolved in a mixture of ethylene glycol and isopropanol with a 1:1 (v/v) ratio. The solution was stirred for 24 h at room temperature, and a milky agglomerate was formed. The obtained material remained for 24 h at room temperature, then the mixture was heated to 70 °C for 24 h, washed with absolute ethanol 3 times (50 mL), and heated to 100 °C for 12 h. Finally, the product was treated to 700 °C at 5 °C min^{-1} in a static air atmosphere to obtain a yellow dust for NiTiO$_3$ and green dust for CoTiO$_3$. For reduced ilmenites, the calcined samples were subjected to a heat treatment for 5 h under pure hydrogen flow at a temperature (500 °C) based on temperature-programmed-reduction (H$_2$-TPR) data.

3.3.2. Characterization Techniques

Specific surface areas were calculated using the Brunauer–Emmett–Teller (BET) method from N$_2$ adsorption–desorption isotherms recorded using a Micromeritics ASAP 2010 instrument. The reduction profile was measured (H$_2$-TPR) for the calcined and reduced

catalysts in a 2900 Micrometrics system equipped with a thermal conductivity detector (TCD). First, data were recorded for 0.05 g of the calcined sample using a 5 vol% H_2/Ar flow of 40 mL min^{-1} heating from room temperature to 800 °C at a rate of 10 °C min^{-1}. Next, the same sample amount was first reduced with pure H_2 at 500 °C, then the temperature was decreased to 100 °C under Ar flow, and a new H_2-TPR was measured under the conditions mentioned. Elemental analysis of the samples was performed by X-ray photoelectron spectroscopy (XPS) (SPECS® spectrometer with a PHOIBOS® 150 WAL) equipped with a hemispherical energy analyzer (resolution < 0.5°) and a μ-FOCUS 500 X-ray monochromator sources, with Al excitation line hν = 1486.6 eV. Binding energy (BE) was corrected with C1s peak (284.9 eV). The structure and crystallinity of calcined and reduced catalysts were determined by X-ray powder diffraction (XRD) with a Ni-filtered Cu Kα1 radiation in a 2θ range of 20°–70° on a Rigaku diffractometer. Refinement by the Rietveld method was performed using FULLPROF software. Experimental patterns, lattice parameters, crystal system, space group, and atomic positions were obtained from the Crystallography Open Database (COD) for the rutile, nickel, and cobalt metal phases. The metallic particle size was estimated using two techniques: transmission electron microscopy (TEM) using JEOL model JEM-1200 EX II microscope and ImageJ software and by applying Sherrer's equation from the width of the X-ray diffraction lines with Gauss broadening.

3.4. Computational Methods

Geometry optimizations for D,L limonene, terpinolene, α-terpinene, γ-terpinene, *p*-cymene, and *p*-cymenene were developed with density functional theory (DFT) using the dispersion wB97XD functional [37] and Def2SVP basis set [38], which are included in the Gaussian 16 package [43]. Molecule geometries of reactants and products were optimized, setting the RMS force criterion to 10^{-5} a.u. The optimized structures were confirmed to be the local minima by estimating the normal vibrations within the harmonic approximation. The reaction pathways were calculated using the synchronous transit-guided quasi-Newton (STQN) method [40], QST2, at the wB97XD/ Def2SVP level of theory.

3.5. Pyrolysis Experiments

An experimental setup for the fast pyrolysis with and without catalysts was performed in an analytical micro-pyrolysis reactor (CDS5200, CDS Analytical, Oxford, USA) connected to a gas chromatograph (GC Perkin Elmer Claurus Cambridge, MA, USA) coupled with a mass spectrometer (MS Perkin Elmer SQ-8T) (Py-GC/MS). For each experiment, 1 (±0.1) mg of sample (waste tire, natural rubber, polybutadiene rubber, and styrene–butadiene rubber) was placed in a quartz tube reactor of 2 cm in length and 2 mm internal diameter, along with the catalyst with a ratio of catalyst-to-tire of 2:1. This ratio was selected to guarantee an adequate response of the used analytic techniques. Quartz wool was placed between the catalyst and tire to avoid direct contact and assign the catalytic effect to purely ex situ operation. To ensure that the reaction products pass through the catalytic bed, it was necessary to put the catalyst on both sides. The reactor was inserted inside a probe and electrically heated using a Pt coil.

The experiments were performed in the temperature range between 400 and 500 °C with a residence time of 12 s, and the heating rate varied with the reaction temperature. High-purity He was used as carrier gas (20mL min^{-1}) to push volatiles into the analysis area (GC/MS). Before entering the GC, volatiles passed by a Tenax trap (pre-column Perkin Elmer), which remained at 280 °C, and then through a heated transfer line (CDS Analytical) were injected to the chromatograph gases. Finally, the reaction products were separated by an Elite 1701 column (30 m × 0.25 mm × 0.25 μm) heated from 45 to 280 °C, with He as the carrier gas at 15 mL min^{-1}. A reactor diagram can be found in Figure S6. The compounds were identified by their mass spectra with an m/z range of 30–600 Da and compared with the NIST MS library. The product distribution was determined by the relative peak area (Area$_{compound(i)}$/Area$_{all\ identified\ compounds}$). Because the tire amount was

strongly controlled, the ratio of relative peak areas can be used as a representation of the selectivity of the products.

4. Conclusions

The catalytic effects of the oxidized and reduced Ni and Co ilmenites on the waste tire pyrolysis were investigated and compared with the non-catalyzed pyrolytic reaction. The results indicated that the uncatalyzed reaction favored the production of D,L-Limonene, and isoprene (~60% and ~25%, respectively) due to the natural rubber depolymerization. Meanwhile, the styrene–butadiene and polybutadiene rubber mainly gave rise to 4-vinylcyclohexene (~80%) by intramolecular cyclization of radical polymer fragments. The target products as BTXs, *p*-cymene, and *p*-cymenene appear in the waste tire and natural rubber in a very low quantity. The computational study showed that limonene isomerization and its subsequent dehydrogenation led to *p*-cymene. In contrast, *p*-cymenene is produced through direct limonene dehydrogenation.

Catalysts promoted secondary reactions resulting in a higher selectivity to BTXs, *p*-cymene, and *p*-cymenene, particularly the reduced Ni-ilmenite-based catalyst. This catalyst enhanced the selectivity of *p*-cymene and *p*-cymenene by 97 and 80%, respectively, compared to the uncatalyzed reaction, while the formation of BTXs was incremented by 70%. The bifunctional character of reduced catalysts favored isomerization and dehydrogenation reactions taking place on D,L-limonene, the main intermediate of the target compounds studied here.

References

1. Tire Industry Project, End-of-Life Tire (ELT) Management Toolkit. Available online: https://www.wbcsd.org/Sector-Projects/Tire-Industry-Project/End-of-Life-Tires-ELTs (accessed on 15 July 2022).
2. WBCSD & The Tire Industry Project, Global ELT Management-A Global State of Knowledge on Regulation, Management Systems, Impacts of Recovery and Technologies. Available online: https://www.wbcsd.org/Sector-Projects/Tire-Industry-Project/End-of-Life-Tires-ELTs (accessed on 15 July 2022).
3. Gao, N.; Wang, F.; Quan, C.; Santamaria, L.; Lopez, G.; Williams, P.T. Tire pyrolysis char: Processes, properties, upgrading and applications. *Prog. Energy Combust. Sci.* **2022**, *93*, 101022–101059. [CrossRef]
4. Arabiourrutia, M.; Lopez, G.; Artetxe, M.; Alvarez, J.; Bilbao, J.; Olazar, M. Waste tyre valorization by catalytic pyrolysis—A review. *Renew. Sustain. Energy Rev.* **2020**, *129*, 109932–109956. [CrossRef]

5. Wang, Z.C.; Duan, P.G.; Wang, K. From waste tire to high value-added chemicals: An analytical Py-GC/TOF–MS study. *Environ. Sci. Pollut. Res.* **2022**, *29*, 72117–72125. [CrossRef]

6. Khalil, U.; Vongsvivut, J.; Shahabuddin, M.; Samudrala, S.P.; Srivatsa, S.C.; Bhattacharya, S. A study on the performance of coke resistive cerium modified zeolite Y catalyst for the pyrolysis of scrap tyres in a two-stage fixed bed reactor. *Waste Manag.* **2020**, *102*, 139–148. [CrossRef] [PubMed]

7. Muenpol, S.; Jitkarnka, S. Effects of Fe supported on zeolites on structures of hydrocarbon compounds and petrochemicals in waste tire-derived pyrolysis oils. *J. Anal. Appl. Pyrolysis* **2016**, *117*, 147–156. [CrossRef]

8. Olazar, M.; Aguado, R.; Arabiourrutia, M.; Lopez, G.; Barona, A.; Bilbao, J. Catalyst effect on the composition of tire pyrolysis products. *Energy Fuels* **2008**, *22*, 2909–2916. [CrossRef]

9. Li, W.; Huang, C.; Li, D.; Huo, P.; Wang, M.; Han, L.; Chen, G.; Li, H.; Li, X.; Wang, Y.; et al. Derived oil production by catalytic pyrolysis of scrap tires, Cuihua Xuebao/Chinese. *J. Catal.* **2016**, *37*, 526–532. [CrossRef]

10. Tavera Ruiz, C.P.; Gauthier-Maradei, P.; Capron, M.; Pirez, C.; Gardoll, O.; Katryniok, B.; Dumeignil, F. Transformation of dl Limonene into Aromatic Compounds Using Supported Heteropolyacid Catalysts. *Catal. Letters.* **2019**, *149*, 328–337. [CrossRef]

11. Dũng, N.A.; Tanglumlert, W.; Wongkasemjit, S.; Jitkarnka, S. Roles of ruthenium on catalytic pyrolysis of waste tire and the changes of its activity upon the rate of calcination. *J. Anal. Appl. Pyrolysis* **2010**, *87*, 256–262. [CrossRef]

12. Yuwapornpanit, R.; Jitkarnka, S. Cu-doped catalysts and their impacts on tire-derived oil and sulfur removal. *J. Anal. Appl. Pyrolysis* **2015**, *111*, 200–208. [CrossRef]

13. Osorio-Vargas, P.; Lick, I.D.; Pizzio, L.R.; Alejandro-Martín, S.; Casas-Ledón, Y.; Poblete, J.; Casella, M.L.; Arteaga-Pérez, L.E. Using tungstophosphoric acid-modified CeO$_2$, TiO$_2$, and SiO$_2$ catalysts to promote secondary reactions leading to aromatics during waste tire pyrolysis. *Mol. Catal.* **2022**, *531*, 112682. [CrossRef]

14. Osorio-Vargas, P.; Shanmugaraj, K.; Herrera, C.; Campos, C.H.; Torres, C.C.; Castillo-Puchi, F.; Arteaga-Pérez, L.E. Valorization of Waste Tires via Catalytic Fast Pyrolysis Using Palladium Supported on Natural Halloysite. *Ind. Eng. Chem. Res.* **2021**, *51*, 18806–18816. [CrossRef]

15. Osorio-Vargas, P.; Menares, T.; Lick, D.; Casella, M.L.; Romero, R.; Jiménez, R.; Arteaga-Pérez, L.E. Tuning the product distribution during the catalytic pyrolysis of waste tires: The effect of the nature of metals and the reaction temperature. *Catal. Today* **2021**, *372*, 164–174. [CrossRef]

16. Osorio-Vargas, P.; Campos, C.H.; Torres, C.C.; Herrera, C.; Shanmugaraj, K.; Bustamante, T.M.; Diaz de Leon, J.; Medina, F.; Arteaga-Pérez, L.E. Catalytic pyrolysis of used tires on noble-metal-based catalysts to obtain high-value chemicals: Reaction pathways. *Catal. Today* **2021**, *394–396*, 475–485. [CrossRef]

17. Williams, P.T.; Brindle, A.J. Catalytic pyrolysis of tyres: Influence of catalyst temperature. *Fuel* **2002**, *81*, 2425–2434. [CrossRef]

18. Muenpol, S.; Yuwapornpanit, R.; Jitkarnka, S. Valuable petrochemicals, petroleum fractions, and sulfur compounds in oils derived from waste tyre pyrolysis using five commercial zeolites as catalysts: Impact of zeolite properties. *Clean Technol. Environ. Policy* **2015**, *17*, 1149–1159. [CrossRef]

19. Williams, P.T.; Brindle, A.J. Aromatic chemicals from the catalytic pyrolysis of scrap tyres. *J. Anal. Appl. Pyrolysis* **2003**, *67*, 143–164. [CrossRef]

20. Buhl, D.; Weyrich, P.A.; Hölderich, W.F. Preparation of p-cymene from mixtures of terpenes as renewable feedstock. *Stud. Surf. Sci. Catal.* **1999**, *121*, 191–196. [CrossRef]

21. Tibbetts, J.D.; Bull, S.D. p-Menthadienes as Biorenewable Feedstocks for a Monoterpene-Based Biorefinery. *Adv. Sustain. Syst.* **2021**, *5*, 2000292. [CrossRef]

22. Tavera-Ruiz, C.; Gauthier-Maradei, P.; Capron, M.; Ferreira-Beltran, D.; Palencia-Blanco, C.; Morin, J.C.; Dumeignil, F. An Alternative to the Cymenes Production from Scrap Tire Rubber Using Heteropolyacid Catalysts. *Waste Biomass Valorization* **2019**, *10*, 3057–3069. [CrossRef]

23. Sun, H.; Xu, X.; Kim, H.; Jung, W.; Zhou, W.; Shao, Z. Electrochemical Water Splitting: Bridging the Gaps between Fundamental Research and Industrial Applications. *Energy Environ. Mater.* **2022**, e12441. [CrossRef]

24. Du, J.; Xiang, D.; Zhou, K.; Wang, L.; Yu, J.; Xia, H.; Zhao, L.; Liu, H.; Zhou, W. Electrochemical hydrogen production coupled with oxygen evolution, organic synthesis, and waste reforming. *Nano Energy* **2022**, *104*, 107875. [CrossRef]

25. Morales, R.; Campos, C.H.; Fierro, J.L.G.; Fraga, M.A.; Pecchi, G. Enhancing xylose aqueous-phase hydrogenation catalytic performance of A-site Ce substituted and B-site Rh doped reduced perovskites. *Mol. Catal.* **2017**, *436*, 182–189. [CrossRef]

26. Pereñiguez, R.; Gonzalez-delaCruz, V.M.; Caballero, A.; Holgado, J.P. LaNiO$_3$ as a precursor of Ni/La$_2$O$_3$ for CO$_2$ reforming of CH 4: Effect of the presence of an amorphous NiO phase. *Appl. Catal. B Environ.* **2012**, *123–124*, 324–332. [CrossRef]

27. Horrillo-Martínez, P.; Virolleaud, M.A.; Jaekel, C. Selective Palladium-Catalyzed Dehydrogenation of Limonene to Dimethyl-styrene. *ChemCatChem* **2010**, *2*, 175–181. [CrossRef]

28. Sanchez-Vazquez, S.A.; Sheppard, T.D.; Evans, J.R.G.; Hailes, H.C. The selective conversion of D-limonene to p,α-dimethylstyrene. *RSC Adv.* **2014**, *4*, 61652–61655. [CrossRef]

29. Williams, P.T.; Besler, S. Pyrolysis- thermogravimetric analysis of tires. *Fuel* **1995**, *74*, 1277–1283. [CrossRef]

30. Miguel, G.S.; Aguado, J.; Serrano, D.P.; Escola, J.M. Thermal and catalytic conversion of used tyre rubber and its polymeric constituents using Py-GC/MS. *Appl. Catal. B Environ.* **2006**, *64*, 209–219. [CrossRef]

31. Thommes, M.; Kaneko, K.; Neimark, A.V.; Olivier, J.P.; Rodriguez-Reinoso, F.; Rouquerol, J.; Sing, K.S.W. Physisorption of gases, with special reference to the evaluation of surface area and pore size distribution (IUPAC Technical Report). *Pure Appl. Chem.* **2015**, *87*, 1051–1069. [CrossRef]

32. González-Vera, D.; Bustamante, T.M.; de León, J.N.D.; Dinamarca, R.; Morales, R.; Osorio-Vargas, P.A.; Torres, C.C.; Campos, C.H. Chemoselective nitroarene hydrogenation over Ni-Pd alloy supported on TiO_2 prepared from ilmenite-type $PdxNi1-xTiO_3$. *Mater. Today Commun.* **2020**, *24*, 101091. [CrossRef]

33. Osorio-Vargas, P.; Flores-González, N.A.; Navarro, R.M.; Fierro, J.L.G.; Campos, C.H.; Reyes, P. Improved stability of Ni/Al_2O_3 catalysts by effect of promoters (La_2O_3, CeO_2) for ethanol steam-reforming reaction. *Catal. Today* **2015**, *259*, 27–38. [CrossRef]

34. Madhavi, J. Comparison of average crystallite size by X-ray peak broadening and Williamson–Hall and size–strain plots for VO^{2+} doped ZnS/CdS composite nanopowder. *SN Appl. Sci.* **2019**, *1*, 1509. [CrossRef]

35. Luo, Y.-R. *Handbook of Bond Dissociation Energies in Organic Compounds*; CRC Press: Boca Raton, FL, USA, 2002; Volume 126. [CrossRef]

36. Golub, M. Thermal rearrangements of unsaturated polymers. *Rubber Chem. Technol.* **1978**, *51*, 677–685. [CrossRef]

37. Chien, J.C.W.; Kiang, J.K. Polymer reactions-x Thermal pyrolysis of poly(isoprene) *. *Eur. Polym. J.* **1979**, *15*, 1059–1065. [CrossRef]

38. Kobe, K.A.; Romans, R.T. Dehydrogenation of p-Cymene. *Ind. Eng. Chem.* **1951**, *43*, 1755–1758. [CrossRef]

39. Corma Canos, A.; Iborra, S.; Velty, A. Chemical routes for the transformation of biomass into chemicals. *Chem. Rev.* **2007**, *107*, 2411–2502. [CrossRef]

40. Busca, G. Metal catalysts for hydrogenations and dehydrogenations. In *Heterogeneous Catalytic Materials*; Elsevier: Amsterdam, The Netherlands, 2014; pp. 297–343. [CrossRef]

41. Osorio-Vargas, P.; Lick, I.D.; Sobrevía, F.; Correa-Muriel, D.; Menares, T.; Manrique, R.; Casella, M.L.; Arteaga-Pérez, L.E. Thermal Behavior, Reaction Pathways and Kinetic Implications of Using a Ni/SiO_2 Catalyst for Waste Tire Pyrolysis. *Waste Biomass Valorization* **2021**, *12*, 6465–6479. [CrossRef]

42. Qu, Y.; Zhou, W.; Fu, H. Porous cobalt titanate nanorod: A new candidate for visible light-driven photocatalytic water oxidation. *ChemCatChem* **2014**, *6*, 265–270. [CrossRef]

43. Frisch, M.J.; Trucks, G.W.; Schlegel, H.B.; Scuseria, G.E.; Robb, M.A.; Cheeseman, J.R.; Scalmani, G.; Barone, V.; Petersson, G.A.; Nakatsuji, H.; et al. *Gaussian 16, Revision, C.01, (n.d.)*; Gaussian, Inc.: Wallingford, CT, USA, 2016.